Temperature Dependence of Lithium Anode Voiding in Argyrodite Solid-State Batteries

Dominic Spencer Jolly [a,b,c,d], *Ziyang Ning* [a,b,c,d], *Gareth O. Hartley* [a,b,c,d], *Boyang Liu* [a,b,c,d], *Dominic Melvin* [a,b,c,d], *Paul Adamson* [a,b,c,d], *James Marrow* [a], *Peter G. Bruce* [a,b,c,d]*

[a] Department of Materials, University of Oxford, Parks Road, Oxford, OX1 3PH, UK

[b] Department of Chemistry, University of Oxford, Parks Road, Oxford, OX1 3PH, UK

[c] The Faraday Institution, Quad One, Becquerel Avenue, Harwell Campus, Didcot, OX11 0RA, UK

[d] The Henry Royce Institute, Parks Road, Oxford, OX1 3PH, UK

Keywords: solid-state battery, lithium anode, interfaces, temperature dependence, X-ray tomography

Abstract

Void formation at the Li/ceramic electrolyte interface of an all-solid-state battery on discharge results in high local current densities, dendrites on charge and cell failure. Here we show that such voiding is reduced at the Li/Li_6PS_5Cl interface at elevated temperature, sufficient to raise the critical current before voiding and cell failure from < 0.25 $mAcm^{-2}$ at 25 °C to 0.25 $mAcm^{-2}$ at 60 °C and 0.5 $mAcm^{-2}$ at 80 °C under a relatively low stack-pressure of 1 MPa. Raising the stack-pressure to 5 MPa and temperature to 80 °C permits stable cycling at 2.5 $mAcm^{-2}$. It is also shown that the charge transfer resistance at the Li/Li_6PS_5Cl interface depends on pressure and temperature, with relatively high pressures required to maintain low charge transfer resistance at -20 °C. These results are consistent with the plastic deformation of Li metal dominating the performance of the Li anode, posing challenges for the implementation of solid-state cells with Li anodes.

Introduction

Lithium metal anodes have the potential to increase the specific energy and energy density of batteries compared with graphite anodes used in state-of-the-art Li-ion cells.[1–7] Coupling Li metal with a ceramic electrolyte is one possible route by which some of the challenges associated with the use of Li in contact with liquid electrolytes might be circumvented.[8–11] However, Li anode solid-state batteries (SSBs) have several major drawbacks including the formation of Li dendrites (filaments penetrating the ceramic) at relatively high rates of charge and voiding in the Li anode at high rates of discharge.[12–21] While significant attention has been given to dendrite growth on charging, the effect of voiding has received less scrutiny until recently, yet the critical current for failure by voiding is often less than that for dendrite formation on charging.[22–24] As a result, the maximum current density at which a solid-state battery can be operated will generally be set by the critical current for voiding.

When the discharge current density of a SSB is sufficiently high that the rate of Li^+ ion transport away from the Li anode exceeds the rate at which Li atoms are replenished at the interface, then voids form in the Li anode at the interface. As shown previously, the extent of voiding increases with cycle number, because not all voids are filled on the subsequent charge and these are added to by new voids on each discharge.[22] The overall effect is diminishing contact between Li and the solid electrolyte on cycling, leading to high local current densities on charge, dendrites and short circuits.[22,25,26] Li transport to the interface can arise from diffusion and plastic deformation (creep). Recent work by Janek and co-workers has explored use of a Li-Mg alloy anode instead of Li metal. Li self-diffusion is greater within the Li-Mg alloy than in Li metal, leading to a higher rate of stable discharge for the Li-Mg anode, however Li diffusivity remains insufficient to enable practical current densities.[27] Other studies have explored the use of stack-pressure to improve transport of

Li to the interface by increasing plastic deformation in the Li metal. It has been shown that higher stack-pressures enable higher rates of discharge in SSBs by inducing higher rates of creep to the Li/SE interface, with the same conclusion also having been drawn for the pressure dependence of the Na/SE interface.[22–25,28–31] Higher temperatures not only increase the rate of self-diffusion within Li metal, but also creep. Dasgupta and co-workers showed that the rate of deformation by power-law creep in Li increases significantly with temperature.[32] As such, SSBs cycled at higher temperature should achieve discharge at higher rates without failures associated with interfacial voiding.

In this study, the morphological stability of the Li/Li_6PS_5Cl interface during discharge is explored over a temperature range of 25 °C to 80 °C. Li_6PS_5Cl is a promising class of solid electrolytes for SSBs with a high ionic conductivity.[22,33–35] 3-Electrode cycling and X-ray computed tomography (XCT) are used to investigate the temperature dependence of the critical current at which voiding occurs on stripping. Under a relatively low stack-pressure of 1 MPa, we demonstrate that at 25 °C the critical current for voiding is exceeded at as little as 0.25 $mAcm^{-2}$ stripping current, the critical current is increased to > 0.25 $mAcm^{-2}$ at 60 °C and > 0.5 $mAcm^{-2}$ at 80 °C. We show that at 80 °C under 5 MPa the highest critical current density that still delivers stable cycling rises by one order of magnitude from < 0.25 $mAcm^{-2}$ at 25 °C and 1 MPa to 2.5 $mAcm^{-2}$. So called ‘anodeless’ or ‘Li-free’ SSBs, in which the Li anode is formed during the first charge, may show somewhat different behaviour, especially polarisation at the very end of stripping all the Li.[36] However higher critical currents at higher temperatures are again to be expected.

Investigation of the temperature and pressure dependence of the interfacial charge transfer resistance reveals that at relatively low temperature (-20 °C), significant pressures of

approximately 12 MPa are required to deform the Li at the interface and avoid high impedances due to poor interfacial contact.

Argyrodite was purchased from AMPCERA and densified into disks of approximately 5 mm diameter and 1 mm thickness by cold-pressing followed by sintering as described in the Experimental Section. 2-Electrode symmetric cells were constructed by contacting with Li disks. When constructing 3-electrode cells, a reference electrode of approximately 1 mm diameter was added to the disk (Figure 1a). Finally, the cells were sealed into pouches and a controlled uniaxial pressure was applied.

How does temperature affect the critical current for voiding?

Cycling 3-electrode cells: temperature dependence under 1 MPa stack-pressure

3-Electrode cells were cycled under 1 MPa pressure at 25 °C, 60 °C and 80 °C. At each temperature, cycling began at 0.25 $mAcm^{-2}$ and the current density was increased in steps of 0.25 $mAcm^{-2}$ every 5 cycles until cell failure. Whereas in the literature most cycling is carried out using symmetric 2-electrode cells to investigate dendrite penetration on charging, the 3-electrode cell enables differentiation between the stripping and plating processes at the Li/SE interface and here we use it to focus on stripping during discharge. It is well established that in 3-electrode cycling, an increase in polarisation during the process of stripping is due to contact loss at the Li/SE interface due to voiding.[22,25,37] Therefore, the critical current density for voiding is determined to be exceeded at currents at which polarisation increases during stripping, Figure 1. As polarisation is much lower on plating than stripping, Figure 1, there is no evidence of increased degradation of Li_6PS_5Cl due to reduction at the Li anode on cycling.

The formation of the SEI layer between Li and Li_6PS_5Cl was studied by PEIS as a function of time at elevated temperature (Figure S1) confirming that the layer growth self-limits at these

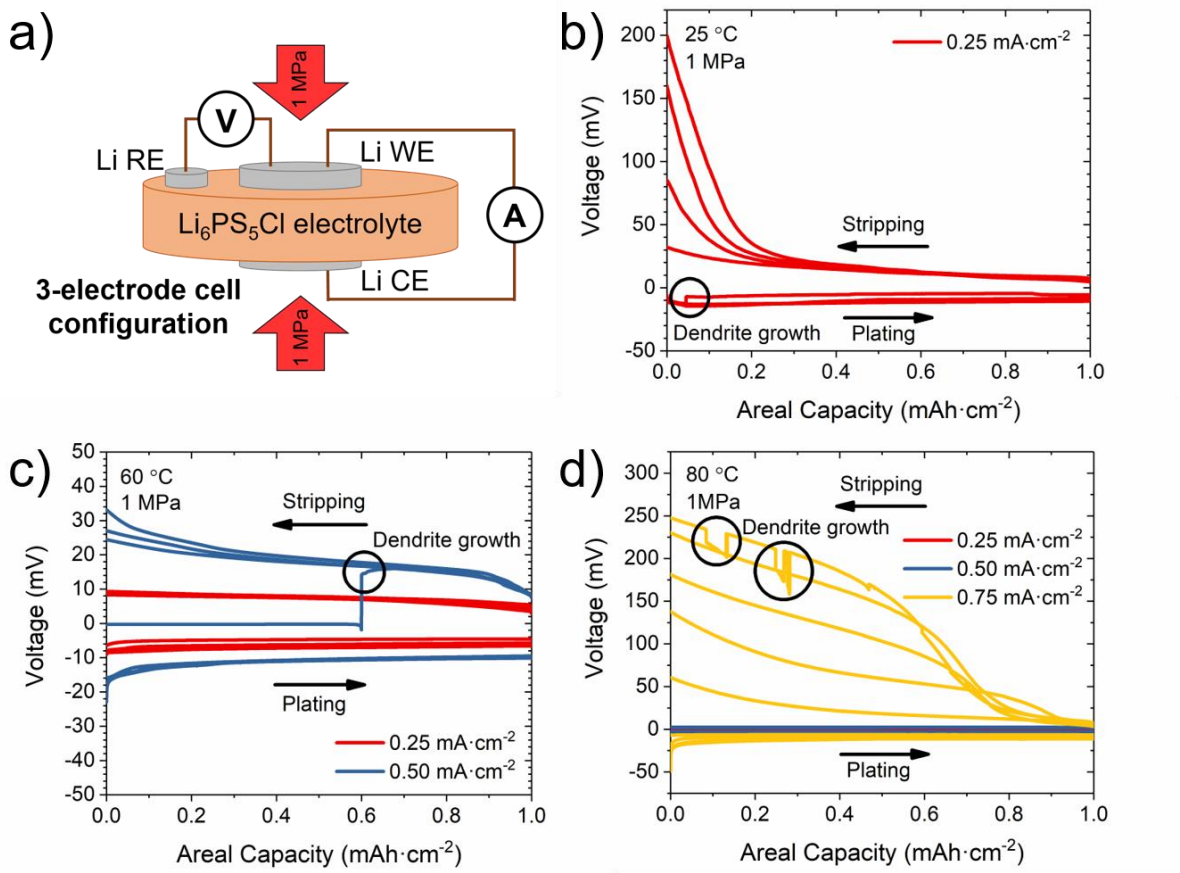

Figure 1: a) Schematic of a 3-electrode Li_6PS_5Cl cell; WE, CE and RE stand respectively for the working, counter and reference electrodes. 3-electrode cycling under 1 MPa pressure moving 1 $mAhcm^{-2}$ capacity at b) 25 °C, c) 60 °C and d) 80 °C. The working electrode was plated first in each case.

elevated temperatures as it does at room temperature. All cycling experiments were carried out on cells that had been rested to ensure formation of a stable SEI.

Considering first the cycling at 25 °C, a polarisation increase of approximately 26 mV is observed during the first stripping of the working electrode at 0.25 $mAcm^{-2}$. By the 4^{th} stripping, polarisation of almost 200 mV is observed, which immediately proceeds cell short-circuit on the 5^{th} plating, indicating dendrite growth across the cell (Figure 1b). At 25 °C and under a low stack-

pressure of 1 MPa, 0.25 $mAcm^{-2}$ already exceeds the critical current for voiding. The loss of contact leads to the high local current densities, dendrites and short-circuit on plating.[22]

By contrast, at the higher temperature of 60 °C (Figure 1c), cycling at 0.25 $mAcm^{-2}$ leads to very similar polarisation on each cycle of ~4 – 8 mV. There is a small increase in voltage at the early stages of stripping on each cycle, which we attribute to minor voiding that is filled on the subsequent plating. This behaviour is in keeping with the fact that we do not expect an abrupt transition from zero voids to voiding that accumulates on each cycle, but rather a transition region where a few small and shallow voids form on stripping that are filled reversibly on plating (red curve). On increasing the current density to 0.5 $mAcm^{-2}$, increasing polarisation is observed on each successive stripping (increasing from 8 mV to 24 mV in the first cycle, to 27 mV in the second cycle and to 33 mV in the third cycle), followed by sudden cell failure due to dendrite growth in the fourth cycle (blue curve). Therefore, at the higher temperature of 60 °C, the critical current density for voiding is greater than 0.25 $mAcm^{-2}$, but is exceeded at 0.5 $mAcm^{-2}$.

Finally, when cycling at 80 °C (Figure 1d), 0.25 $mAcm^{-2}$ again shows no increase in polarisation on stripping, maintaining a stable voltage (red curve). Upon increasing the current density to 0.5 $mAcm^{-2}$, cycling remains highly reversible, maintaining a stable voltage (blue curve). However, on increasing the current density to 0.75 $mAcm^{-2}$, the cell immediately exhibits severe void formation on stripping (yellow curve), with the voltage increasing from ~6 mV to 61 mV during the first stripping and reaching a polarisation of 248 mV during the fifth stripping, by which time the cell shows clear signs of dendrite growth, evidenced by the fluctuations in the voltage curve on stripping, features that have been discussed previously.[38–40] Therefore, at 80 °C, whilst 0.5 $mAcm^{-2}$ is below the critical current for void formation, 0.75 $mAcm^{-2}$ clearly exceeds this critical value at 1 MPa pressure.

Imaging voids: Tomography of the Li/Li_6PS_5Cl interface

Morphological changes at the Li/SE interface on cycling were followed by XCT. 2-Electrode symmetric cells were cycled at 80 °C under 1 MPa pressure at 0.5 $mAcm^{-2}$ and 0.75 $mAcm^{-2}$ i.e. below and above the critical current for voiding determined in Figure 1d. The cells were imaged after 25 cycles or following failure. In line with the 3-electrode results, a cell cycled at 0.5 $mAcm^{-2}$ at 80 °C and under 1 MPa pressure showed highly reversible cycling with little change in voltage (Figure 2b), consistent with the absence of voiding during stripping. This result was supported by XCT imaging, which showed little difference between the Li/Li_6PS_5Cl interface following the 25^{th} stripping (Figure 2e) and a pristine cell (Figure 2d). Good contact was seen between the Li electrode (green) and the solid electrolyte (yellow) in both. The one area of blue, indicative of a void, in Figure 2e represents only ~3 % of the electrode/electrolyte interface. On the other hand, when a cell is cycled at 0.75 $mAcm^{-2}$ under the same conditions, increasing polarisation is observed over 12 cycles (Figure 2c) and voids (blue) are apparent across the entire interface between the Li electrode and the solid electrolyte (Figure 2f). The cell ultimately short-circuits on the 13^{th} plating, indicating Li dendrite growth across the electrolyte as shown in Figure S3.

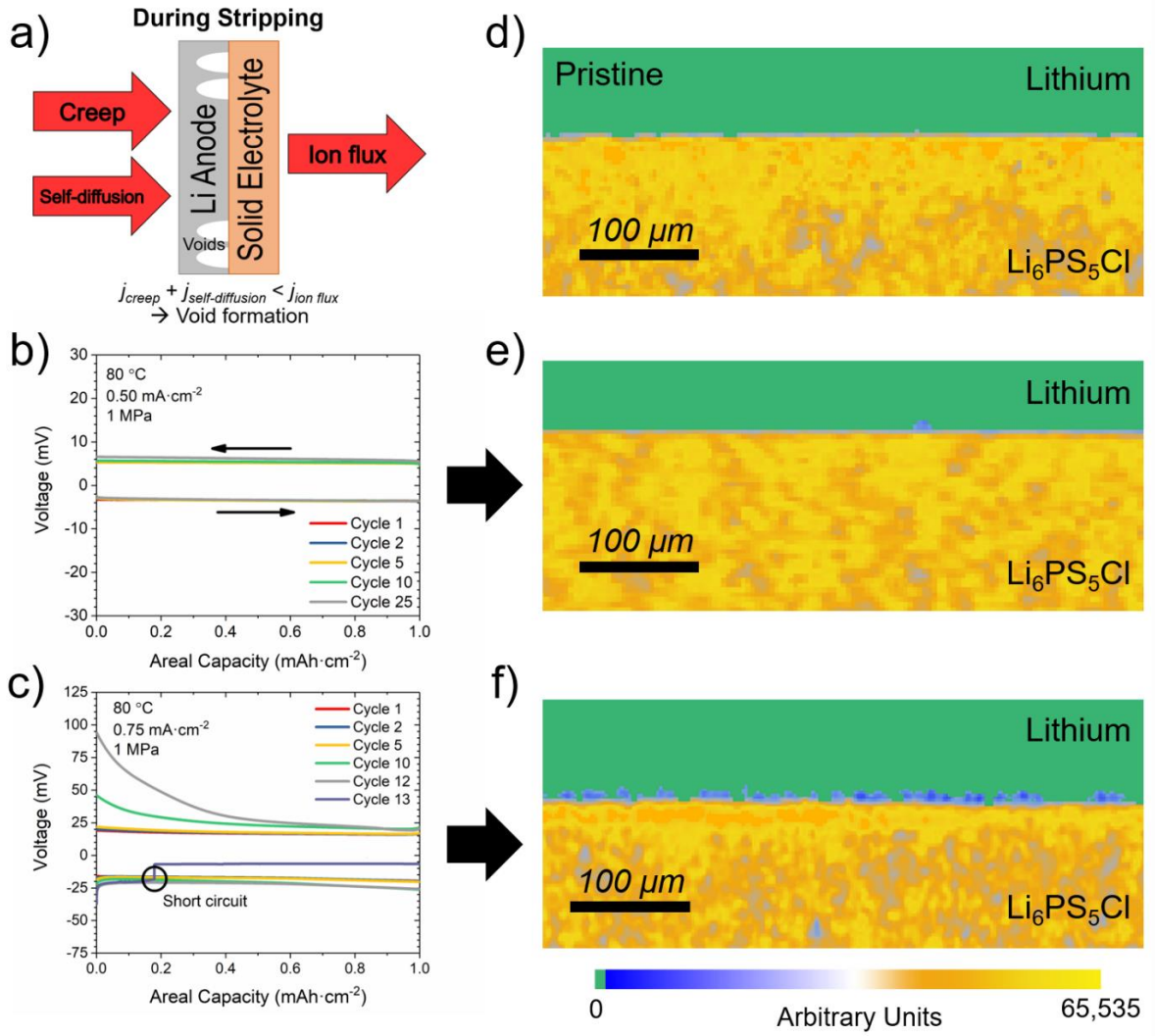

Figure 2: a) Schematic showing the condition for void formation in the Li anode. 2-Electrode cycling at 80 °C under 1 MPa at b) 0.5 mAcm^{-2} and c) 0.75 mAcm^{-2}; X-ray tomography cross-sectional images of the Li/Li_6PS_5Cl interface for d) pristine cell and e) after cycling at 0.5 mAcm^{-2} corresponding to (b) and f) 0.75 mAcm^{-2} corresponding to (c). Green, blue and orange/yellow indicate lithium, voids and Li_6PS_5Cl respectively. The values and associated colour scale correspond physically to the X-ray attenuation and therefore the scattering by the constituent atoms. Unsegmented XCT images are shown in Figure S2.

Influence of pressure and temperature on the charge transfer resistance

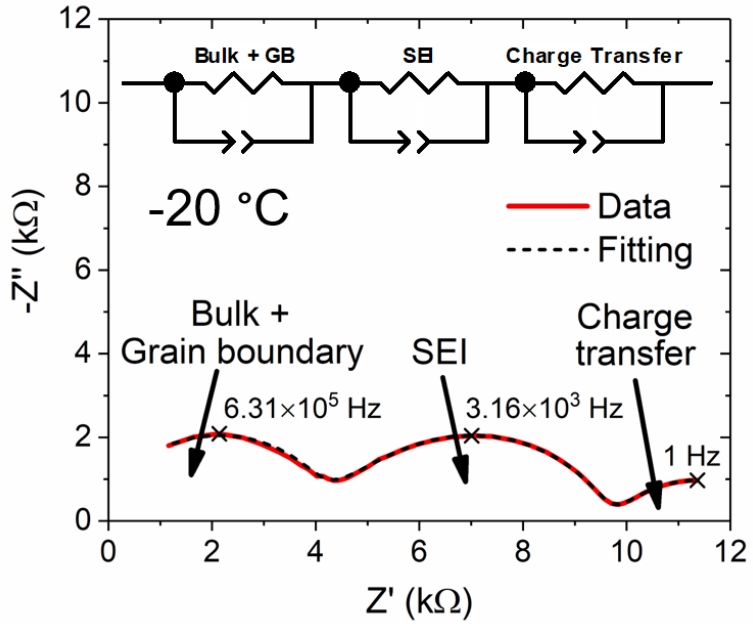

Figure 3: Nyquist plot of a Li/Li_6PS_5Cl/Li cell at -20 °C and 1 MPa stack-pressure, showing the experimental data (red) and the fitting from the equivalent circuit model (black). The bulk and grain boundary, SEI and charge transfer contributions are identified.

The importance of the mechanical properties of Li, and hence their temperature dependence, not only applies to the dynamic Li/SE interface during cycling, but also to the static Li/SE interface of a cell at rest. Previous work by Janek and co-workers used potentiostatic electrochemical impedance spectroscopy (PEIS) to show that the interfacial impedance of the Li/LLZO interface decreases with increasing stack-pressure, becoming very small at very high pressures and related to constriction of current due to imperfect contact at the interface which reduces as Li yields under high pressure.[23] Before investigating the Li/Li_6PS_5Cl interface it is necessary to assign the features in the PEIS spectrum. PEIS of a 2-electrode Li/Li_6PS_5Cl/Li cell was conducted at -20 °C and is shown as a Nyquist plot in Figure 3. The spectrum was modelled as three parallel RC elements in series, which were assigned, from high to low frequency, as bulk and grain boundary, solid

R/C Element	Resistance	Capacitance
Bulk + Grain boundary	2901 Ωcm	8.7×10^{-11} Fcm^{-1}
SEI	402 Ωcm^2	1.2×10^{-7} Fcm^{-2}
Charge Transfer	229 Ωcm^2	7.0×10^{-4} Fcm^{-2}

Table 1: Table showing normalised resistances and capacitances from the equivalent circuit model fitting of a 2-electrode Li/Li_6PS_5Cl/Li cell at -20 °C

electrolyte interphase (SEI) and interfacial charge transfer impedances respectively according to their capacitances, which are shown in Table 1.[41] The bulk and grain boundary phenomena could not be deconvoluted and so were modelled together, as in previous literature on argyrodite solid electrolytes.[42,43] Further PEIS measurements were made in 10 °C steps up to 80 °C and these are shown in Figure S4a. The associated Arrhenius plots are shown in Figures S4b-c and give activation energies of 0.36 eV for bulk + grain boundary and of 0.45 eV for the SEI, in good accord with the literature.[44–47] It has been shown that on contacting Li_6PS_5Cl with Li, the former is reduced resulting in a layer of predominantly Li_2S beteeen the solid electrolyte and Li. The growth stops rapidly and the layer acts as a passivating SEI, stabilising the interface.[22,33] We assign the SEI impedance to this layer. As a result, the charge transfer impedance at the inteface is between Li_2S and the Li electrode.

The effect of stack-pressure on the interfacial charge transfer resistance at different temperatures is shown in Figure 4a, where an initial significant decrease is followed by a continuous plateau up to high pressure. This indicates that at 25 °C Li behaves plastically and deforms even at low stack pressures, a finding which is consistent with the low yield strength of Li at room-temperature (σ_{Li} = 0.73-0.81 MPa).[48] Figure 4b shows the pressure dependence of impedance at the lower temperature of -20 °C. Again there is a decrease in the charge transfer resistance at the interface, this time across a much wider pressure range than was observed at room-temperature, with no

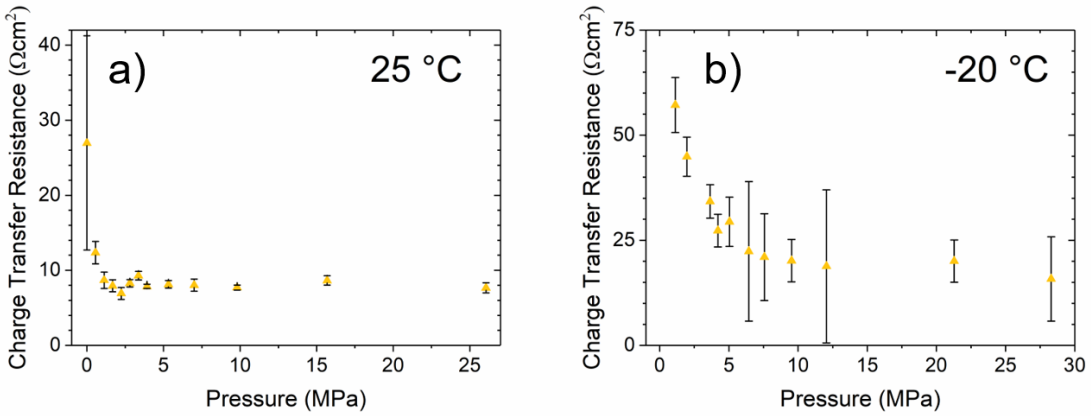

Figure 4: The pressure dependence of charge transfer resistance at the interface at a) 25 °C and b) -20 °C. Note that the error bars give the error in the least-squares fitting of the charge transfer resistance contribution only.

plateau evident until a pressure of approximately 12 MPa. This is consistent with decreased deformation of Li at lower temperature, with higher stack pressures required to achieve the same Li/SE contact. High temperatures not only aid in maintaining interfacial contact during the dynamic process of stripping on cell discharge, but also decrease the charge transfer resistance. Furthermore, the results show that operating a battery based on Li_6PS_5Cl and a Li anode becomes problematical at low temperatures unless high pressures are used. As well as the charge transfer resistance decreasing with pressure, so too does the bulk + grain boundary resistance, as shown in Figure S7. By contrast, the SEI resistance shows much less change with pressure, suggesting the decreasing resistance of the Li_6PS_5Cl ceramic could be due to reduced intergranular resistances in this pressure range.

As seen in Figure 3, the charge transfer is not the largest resistance in the cell. In a practical cell the solid electrolyte would be thinner and therefore the bulk and grain boundary resistances smaller. However the important point is that the charge transfer resistance grows when stripping under insufficient stack-pressure which leads to cell failure.

It interesting to note that the data presented here are a close match to the inverse pressure dependence of interfacial resistance under conditions in which Li is plastically deforming (Figure S5) as predicted in the theoretical work of Harris and co-workers.[29] The stack-pressure dependence of the Li/Li_6PS_5Cl interface was also investigated at 80 °C (Figure S6c). However, at this high temperature, the relative magnitude of the interfacial contribution to the impedance, compared with those of bulk and grain boundary, meant that errors in least-squares fitting were high and that no change in interfacial resistance of any statistical significance was observed.

High critical current for voiding at moderate temperature and pressure

The above data show that morphologically stable cycling at 0.5 $mAcm^{-2}$ is possible at 80 °C under 1 MPa. Previous research showed that only 0.2 $mAcm^{-2}$ under 3.5 MPa and 1 $mAcm^{-2}$ under 7 MPa was attainable at room temperature.[22] Operating batteries at high pressures or temperatures is unlikely to be viable in practice. Could a combination of moderate temperature and stack pressure prove an effective strategy for achieving relatively high current densities for cycling?

In Figure 5, 3-electrode cycling is used to determine the critical current density for voiding on stripping at a stack-pressure of 5 MPa. Cycling commenced at 0.25 $mAcm^{-2}$ and the current density was increased in steps of 0.25 $mAcm^{-2}$ every 5 cycles to 1 $mAcm^{-2}$, then increased in steps of 0.5 $mAcm^{-2}$ until cell failure. For clarity, only key current densities are shown in Figure 5, with complete cycling data shown in Figure S8. At a temperature of 25 °C (Figure 5a), the cell showed no increase in polarisation and maintained a low and stable polarisation when cycling at current densities up to and including 0.75 $mAcm^{-2}$ (yellow curve). This indicates that up to a current density of 0.75 $mAcm^{-2}$, little or no voiding occurs on cycling. However, when cycling at 1 $mAcm^{-2}$ some polarisation on stripping is observed, with the voltage increasing by 28 mV at the end of

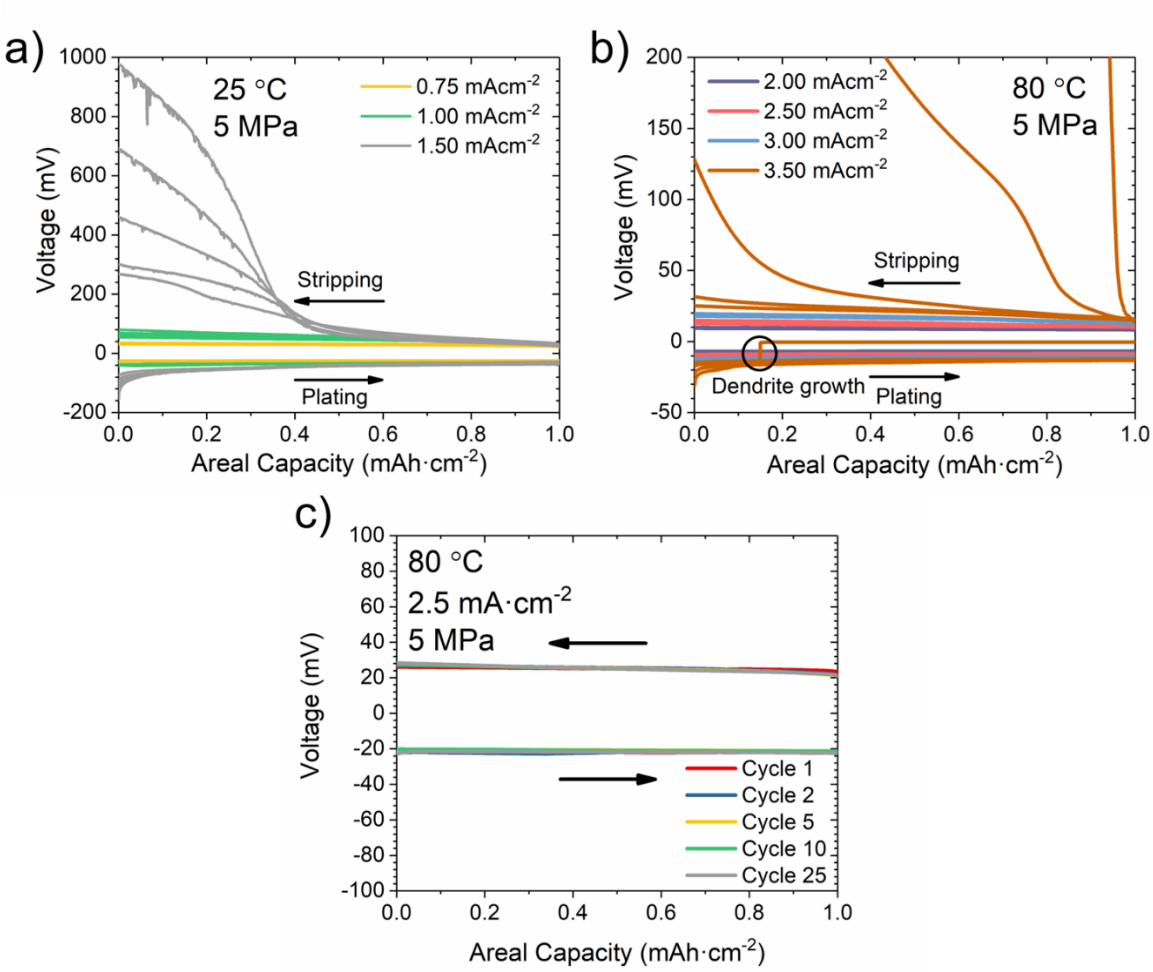

Figure 5: 3-Electrode cycling under 5 MPa pressure moving 1 mAhcm^{-2} capacity at a) 25 °C, and b) 80 °C. Complete voltage profiles for these cells are shown in Figure S8, including additional current densities. Cell cycling began by plating the working electrode in each case. c) Cycling of a 2-electrode Li/Li_6PS_5Cl/Li symmetric cell at 2.5 mAcm^{-2} at 80 °C under 5 MPa stack-pressure, showing highly reversible plating and stripping over 25 cycles.

the 1st stripping and to 54 mV by the end of the 5th stripping (green curve), indicating irreversible void formation. At 1.5 mAcm^{-2} (grey curve), polarisation on stripping is severe, and stochastic variation in the cell voltage provides the first indication of dendrite growth through the ceramic separator.[38–40] While total cell failure did not occur until 2.5 mAcm^{-2}, it is clear that the critical current density for voiding on stripping had been exceeded at 1 mAcm^{-2}.

When cycling under a 5 MPa stack-pressure at an elevated temperature of 80 °C, little cell polarisation was observed at low and moderately high current densities, with stripping at current densities up to and including 2.5 $mAcm^{-2}$ (pink curve) maintaining low and stable potential, (Figure 5b). At 3.0 $mAcm^{-2}$ (light blue curve), a very slight voltage increase is observed over 5 cycles, indicating some void formation, but it is not until 3.5 $mAcm^{-2}$ (brown curve) that severe polarisation is observed, with the voltage reaching 0.55 V by the end of the 4^{th} charge. This results shows that under a stack-pressure of 5 MPa and temperature of 80 °C, the critical current density has increased significantly to 2.5 $mAcm^{-2}$.

In order to confirm that the Li/SE interface can be reversibly cycled at a high current density over an extended period, a 2-electrode cell was cycled at 2.5 $mAcm^{-2}$ under a 5 MPa stack pressure at 80 °C. As shown in Figure 5c, the cell had a stable voltage profile throughout, showing no polarisation increase over 25 cycles. It is clearly beneficial to cycle under higher stack-pressures, however it must be acknowledged that there are challenges associated with up-scaling pressures from small footprint laboratory-scale cells to larger footprint batteries, with challenges including ensuring even pressure and preventing lateral flow in larger cells.[48]

Importance of continuous stack-pressure

This work emphasises the importance of Li metal creep to the Li/Li_6PS_5Cl interface and therefore continuous stack pressure during cell discharge. To demonstrate this further, a Li/Li_6PS_5Cl/Li symmetric cell was constructed by pressing Li electrodes onto a cold-pressed Li_6PS_5Cl disk under 100 MPa of pressure in a PEEK cell. The pressure was released and the cell cycled under no stack-pressure at 80 °C, increasing the current density every 5 cycles (Figure 6). The cell initially showed stable potential at the low current density of 0.25 $mAcm^{-2}$ (red curve),

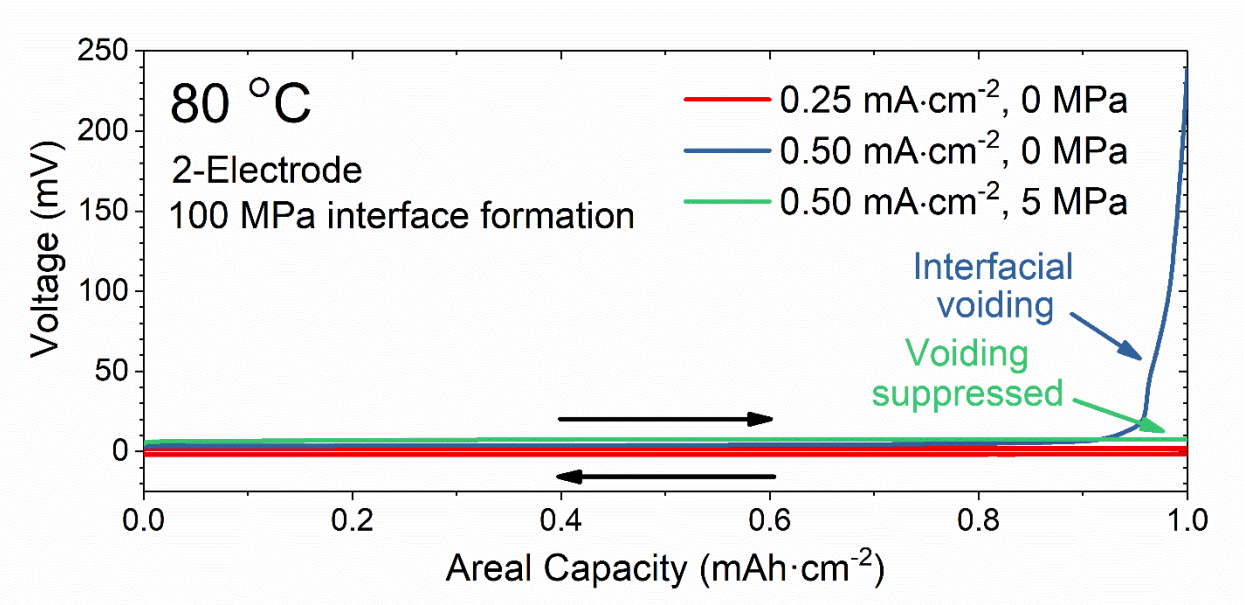

Figure 6: Cycling of a 2-electrode Li/Li_6PS_5Cl/Li symmetric cell made under 100 MPa formation pressure. Cycling was initially carried out under no stack-pressure. Voltage was stable for 5 cycles at 0.25 $mAcm^{-2}$ (red curve) but severe polarisation was observed at 0.5 $mAcm^{-2}$ (blue curve). The interface was subsequently recovered by re-pressing at 100 MPa. The cell was then cycled under 5 MPa stack-pressure, achieving stable potential (green curve).

indicating that at low current densities self-diffusion in the Li is sufficient to prevent interfacial voiding. At the higher current density of 0.5 $mAcm^{-2}$, the cell shows polarisation due to voiding in the first half-cycle (blue curve), giving a critical current for voiding significantly below the 2.5 $mAcm^{-2}$ current density observed under 5 MPa stack-pressure (Figure 5b). In order to demonstrate that this failure can be prevented by a continuous stack-pressure, the same cell was re-pressed under 100 MPa to eliminate the interfacial voids, reforming the Li/Li_6PS_5Cl interface. The cell was then placed under a 5 MPa stack-pressure and a half-cycle was carried out at the same current density (green curve), this time giving a stable voltage. It can therefore be concluded that using high pressures to form the interface does not prevent interfacial voiding at even moderate current densities, in agreement with previous work,[49] and that to achieve discharge current densities up to

the 2.5 $mAcm^{-2}$ under 5 MPa at 80 °C reported in this work, continuous stack-pressures are required.

Conclusion

Operating a solid-state battery with a Li anode at elevated temperatures increases the critical current at which voids form. The critical current density for void formation on cycling at the Li/Li_6PS_5Cl interface increases from < 0.25 $mAcm^{-2}$ at 25 °C, to > 0.5 $mAcm^{-2}$ at 80 °C when cycling under 1 MPa pressure. However, this increases to 2.5 $mAcm^{-2}$ at 80 °C under 5 MPa stack-pressure, approaching cycling rates of interest for practical solids state batteries.

These results are in accord with Li creep dominating Li transport to the interface. The charge transfer resistance at the Li/Li_6PS_5Cl interface depends strongly on temperature and pressure, in accord with the role of Li plastic deformation being a dominant process.

Experimental Section

Preparation of Li_6PS_5Cl Disks: Li_6PS_5Cl powder was purchased from AMPCERA and densified into disks of 5 mm diameter and approximately 1 mm thickness by uniaxial pressing at 1 t. Following pressing, the disks were transferred to a furnace, where they were sintered at 300 °C for 30 min. All preparation was conducted inside an Ar-filled glovebox (< 1 ppm O_2 and H_2O). Li_6PS_5Cl powder was characterised by Powder X-ray Diffraction (PXRD), shown in Figure S9, which indicated good purity of the Li_6PS_5Cl cubic phase.[22,50]

Li/Li_6PS_5Cl/Li Cell Assembly: Two types of cell were used in this study: 1) pouch cells for single-pressure testing and 2) PEEK cells for variable pressure testing. 2-Electrode pouch cells were constructed by punching disks of Li 3 mm in diameter and approximately 50 um thick from Li foil and affixing them to the Li_6PS_5Cl disks using uniaxial pressure. 3-Electrode cells were made by the addition of a further 1 mm diameter Li disk as the reference electrode, alongside the working electrode, as described previously.[22] These were sealed under vacuum within a pouch with Cu current collectors. All cells were placed under pressure at 80 °C overnight prior to cycling to improve the Li/Li_6PS_5Cl contacts at the interfaces, except for that used for assignment of the Nyquist plot (Figure 3) which was placed directly under 1 MPa pressure. All cells were rested for at least 24 h prior to cycling to allow for a stable SEI layer to form at the Li/Li_6PS_5Cl interface. PEEK cells were used for the variable pressure PEIS measurements. These cells were all 2-electrode and used 5 mm Li electrodes.

Temperatures were controlled to ± 0.02 °C using temperature control chambers (Huber) within a glovebox (MBRAUN). Pressures were set using a custom load cell with a piezoelectric pressure sensor as described in previous work.[22]

Galvanostatic Cycling and PEIS: Galvanostatic cycling and PEIS were performed using Gamry Interface 1010 E potentiostats. The areal capacity for galvanostatic cycling was fixed at 1 $mAhcm^{-2}$ throughout this study and cycling always began with plating at the working electrode and stripping at the counter electrode. PEIS was performed using a voltage perturbation of 5 mV in a frequency range of 1 MHz to 1 Hz unless otherwise specified, collecting 10 points per decade. Temperature was controlled within a temperature control chamber as described previously. PEIS spectra were fitted using an equivalent circuit model on the ZView software package.

X-ray Computed Tomography:

The cycled cells were disassembled and sealed into pouches for imaging in an Ar-filled glovebox. X-ray tomograms were recorded within a Zeiss Xradia Versa 510 X-ray computed tomography microscope at 80 kV accelerating voltage and current of 87.5 µA. For each tomogram, 2401 equiangularly distributed projections were taken over 360° with a resulting pixel size of 1.99 µm/voxel.

The tomograms were reconstructed using Zeiss Scout and Scan Control System Reconstructor into 16-bit tiff images. The tiff images were resliced perpendicular to the Li/SE interface, and cropped to show the voids at the Li/SE interface. The resliced images were then processed using Avizo Fire. The 16-bit Hounsfield grayscale image was filtered with non-local means filter first, then, then with lithium electrode, voids & Li_6PS_5Cl electrolyte segmented out with interactive thresholding, respectively. With the grayscale of lithium electrode set to zero, and the grayscale of voids and Li_6PS_5Cl electrolyte unchanged, a customised diverging colour-map was applied to the resliced images to enhance the contrast between voids and lithium electrode.

Powder X-ray Diffraction:

PXRD was carried out using a Rigaku MiniFlex 600 instrument with Cu $K\alpha_1$ radiation in a glovebox with a nitrogen atmosphere. A powder sample was placed onto a low background single crystal silicon sample holder and the diffraction pattern was collected over a 2θ range of 15 ° to 90 °.

Associated Content

The supporting information is available free of charge.

Supporting Figures S1-9: PEIS showing SEI formation at 80 °C; Unsegmented XCT images of pristine cell and after cycling; XCT cross-section showing voiding and dendrite growth; Nyquist and Arrhenius plots showing temperature dependence of Li/Li_6PS_5Cl/Li impedance; Plot showing dependence of charge transfer resistance on pressure; Nyquist plots showing temperature and pressure dependence of a cell at rest; Plot showing temperature and pressure dependence of bulk + grain boundary and SEI resistances; Full cycling data under 5 MPa stack-pressure; PXRD of Li_6PS_5Cl.

Corresponding Author

* Email: peter.bruce@materials.ox.ac.uk

Author Contributions

D.S.J. contributed to all aspects of the research. Z.N. carried out XCT experiments. B.L. helped with high formation pressure experiments. D.M. carried out PXRD. D.S.J., Z.N., G.O.H., B.L., D.M., P.A., J.M. and P.G.B. analysed the data. D.S.J. and P.G.B. wrote the paper. The project was supervised by P.G.B.

Acknowledgements

P.G.B. is indebted to the Engineering and Physical Sciences Research Council (EPSRC), [EP/M009521/1], Henry Royce Institute for Advanced Materials [EP/R00661X/1, EP/S019367/1, EP/R010145/1] and the Faraday Institution [FIRG007, FIRG008] for financial support. The X-ray tomography facilities were funded by EPSRC Grant [EP/M02833X/1] "University of Oxford: experimental equipment upgrade".

TOC Image:

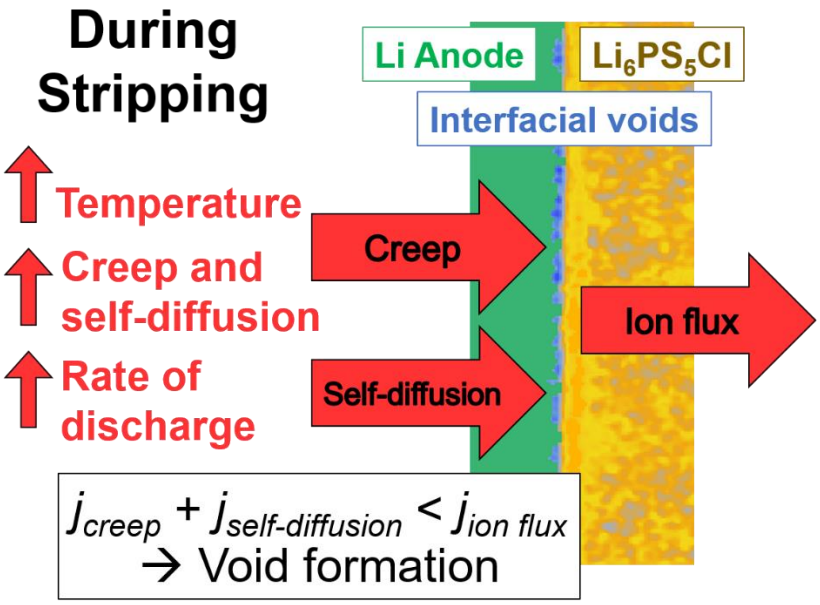

References

(1) Busche, M. R.; Drossel, T.; Leichtweiss, T.; Weber, D. A.; Falk, M.; Schneider, M.; Reich, M. L.; Sommer, H.; Adelhelm, P.; Janek, J. Dynamic Formation of a Solid-Liquid Electrolyte Interphase and Its Consequences for Hybrid-Battery Concepts. *Nat. Chem.* **2016**, *8* (5), 426–434. https://doi.org/10.1038/nchem.2470.

(2) Famprikis, T.; Canepa, P.; Dawson, J. A.; Islam, M. S.; Masquelier, C. Fundamentals of Inorganic Solid State Electrolytes for Batteries. *Nat. Mater.* **2019**. https://doi.org/10.1038/s41563-019-0431-3.

(3) Tarascon, J. M.; Armand, M. Issues and Challenges Facing Rechargeable Lithium Batteries. *Nature* **2001**, *414* (6861), 359–367. https://doi.org/10.1038/35104644.

(4) Goodenough, J. B.; Kim, Y. Challenges for Rechargeable Li Batteries. *Chem. Mater.* **2010**, *22* (3), 587–603. https://doi.org/10.1021/cm901452z.

(5) Shen, X.; Li, Y.; Qian, T.; Liu, J.; Zhou, J.; Yan, C.; Goodenough, J. B. Lithium Anode Stable in Air for Low-Cost Fabrication of a Dendrite-Free Lithium Battery. *Nat. Commun.* **2019**, *10* (1). https://doi.org/10.1038/s41467-019-08767-0.

(6) Liu, J.; Bao, Z.; Cui, Y.; Dufek, E. J.; Goodenough, J. B.; Khalifah, P.; Li, Q.; Liaw, B. Y.; Liu, P.; Manthiram, A.; Shirley Meng, Y.; Subramanian, V. R,; Toney, M. F.; Viswanathan, V. V.; Whittingham, M. S.; Xiao, J.; Xu, W.; Yang, J.; Yang, X.; Zhang, J. Pathways for Practical High-Energy Long-Cycling Lithium Metal Batteries. *Nat. Energy* **2019**, *4* (3), 180–186. https://doi.org/10.1038/s41560-019-0338-x.

(7) Fang, C.; Wang, X.; Meng, Y. S. Key Issues Hindering a Practical Lithium-Metal Anode.

Trends Chem. **2019**, *1* (2), 152–158. https://doi.org/10.1016/j.trechm.2019.02.015.

(8) Bieker, G.; Winter, M.; Bieker, P. Electrochemical in Situ Investigations of SEI and Dendrite Formation on the Lithium Metal Anode. *Phys. Chem. Chem. Phys.* **2015**, *17* (14), 8670–8679. https://doi.org/10.1039/c4cp05865h.

(9) Placke, T.; Kloepsch, R.; Dühnen, S.; Winter, M. Lithium Ion, Lithium Metal, and Alternative Rechargeable Battery Technologies: The Odyssey for High Energy Density. *J. Solid State Electrochem.* **2017**, *21* (7), 1939–1964. https://doi.org/10.1007/s10008-017-3610-7.

(10) Lin, D.; Liu, Y.; Cui, Y. Reviving the Lithium Metal Anode for High-Energy Batteries. *Nat. Publ. Gr.* **2017**, *12*. https://doi.org/10.1038/NNANO.2017.16.

(11) Banerjee, A.; Wang, X.; Fang, C.; Wu, E. A.; Meng, Y. S. Interfaces and Interphases in All-Solid-State Batteries with Inorganic Solid Electrolytes. *Chem. Rev.* **2020**, *120* (14), 6878–6933. https://doi.org/10.1021/acs.chemrev.0c00101.

(12) Krauskopf, T.; Richter, F. H.; Zeier, W. G.; Janek, J. Physicochemical Concepts of the Lithium Metal Anode in Solid-State Batteries. *Chem. Rev.* **2020**. https://doi.org/10.1021/acs.chemrev.0c00431.

(13) Xiao, Y.; Wang, Y.; Bo, S. H.; Kim, J. C.; Miara, L. J.; Ceder, G. Understanding Interface Stability in Solid-State Batteries. *Nat. Rev. Mater.* **2020**, *5* (2), 105–126. https://doi.org/10.1038/s41578-019-0157-5.

(14) Pasta, M.; Armstrong, D.; Brown, Z. L.; Bu, J.; Castell, M. R.; Chen, P.; Cocks, A.; Corr, S. A.; Cussen, E. J.; Darnbrough, E.; Deshpande, V.; Doerrer, C.; Dyer, M. S.; El-Shinawi,

H.; Fleck, N,; Grant, P.; Gregory, G. L.; Grovenor, C.; Hardwick, L. J.; Irvine, J. T. S.; Lee, H. J.; Li, G.; Liberti, E.; McClelland, I.; Monrow, C.; Nellist, P. D.; Shearing, P. R.; Shoko, E.; Song, W.; Spencer Jolly, D.; Thomas, C. I.; Turrell, S. J.; Vestli, M.; Williams, C. K.; Zhou, Y.; Bruce, P. G. 2020 Roadmap on Solid-State Batteries. *J. Phys. Energy* **2020**, *2*, 0–52.

(15) Kerman, K.; Luntz, A.; Viswanathan, V.; Chiang, Y.-M.; Chen, Z. Review - Practical Challenges Hindering the Development of Solid State Li Ion Batteries. *J. Electrochem. Soc.* **2017**, *164* (7), A1731–A1744. https://doi.org/10.1149/2.1571707jes.

(16) Porz, L.; Swamy, T.; Sheldon, B. W.; Rettenwander, D.; Frömling, T.; Thaman, H. L.; Berendts, S.; Uecker, R.; Carter, W. C.; Chiang, Y. M. Mechanism of Lithium Metal Penetration through Inorganic Solid Electrolytes. *Adv. Energy Mater.* **2017**, *7* (20), 1–12. https://doi.org/10.1002/aenm.201701003.

(17) Aguesse, F.; Manalastas, W.; Buannic, L.; Del Amo, J. M. L.; Singh, G.; Llordés, A.; Kilner, J. Investigating the Dendritic Growth during Full Cell Cycling of Garnet Electrolyte in Direct Contact with Li Metal. *ACS Appl. Mater. Interfaces* **2017**, *9* (4), 3808–3816. https://doi.org/10.1021/acsami.6b13925.

(18) Cheng, E. J.; Sharafi, A.; Sakamoto, J. Intergranular Li Metal Propagation through Polycrystalline $Li_{6.25}Al_{0.25}La_3Zr_2O_{12}$ Ceramic Electrolyte. *Electrochim. Acta* **2017**, *223*, 85–91. https://doi.org/10.1016/j.electacta.2016.12.018.

(19) Marbella, L. E.; Zekoll, S.; Kasemchainan, J.; Emge, S. P.; Bruce, P. G.; Grey, C. P. ^{7}Li NMR Chemical Shift Imaging to Detect Microstructural Growth of Lithium in All-Solid-State Batteries. *Chem. Mater.* **2019**, *31* (8), 2762–2769.

https://doi.org/10.1021/acs.chemmater.8b04875.

(20) Rees, G. J.; Spencer Jolly, D.; Ning, Z.; Marrow, T. J.; Pavlovskaya, G.; Bruce, P. G. Imaging Sodium Dendrite Growth in All-Solid-State Sodium Batteries Using ^{23}Na T2-weighted MRI. *Angew. Chemie Int. Ed.* **2020**, 1–7. https://doi.org/10.1002/anie.202013066.

(21) Hatzell, K. B.; Chen, X. C.; Cobb, C. L.; Dasgupta, N. P.; Dixit, M. B.; Marbella, L. E.; McDowell, M. T.; Mukherjee, P. P.; Verma, A.; Viswanathan, V.; Westover, A. S.; Zeier, W. G. Challenges in Lithium Metal Anodes for Solid-State Batteries. *ACS Energy Lett.* **2020**, *5* (3), 922–934. https://doi.org/10.1021/acsenergylett.9b02668.

(22) Kasemchainan, J.; Zekoll, S.; Spencer Jolly, D.; Ning, Z.; Hartley, G. O.; Marrow, J.; Bruce, P. G. Critical Stripping Current Leads to Dendrite Formation on Plating in Lithium Anode Solid Electrolyte Cells. *Nat. Mater.* **2019**, *18*, 1105–1111. https://doi.org/10.1038/s41563-019-0438-9.

(23) Krauskopf, T.; Hartmann, H.; Zeier, W. G.; Janek, J. Toward a Fundamental Understanding of the Lithium Metal Anode in Solid-State Batteries - An Electrochemo-Mechanical Study on the Garnet-Type Solid Electrolyte $Li_{6.25}Al_{0.25}La_3Zr_2O_{12}$. *Appl. Interfaces Mater.* **2019**, No. 11, 14463–14477. https://doi.org/10.1021/acsami.9b02537.

(24) Wang, M. J.; Choudhury, R.; Sakamoto, J. Characterizing the Li-Solid-Electrolyte Interface Dynamics as a Function of Stack Pressure and Current Density. *Joule* **2019**, 1–14. https://doi.org/10.1016/j.joule.2019.06.017.

(25) Spencer Jolly, D.; Ning, Z.; Darnbrough, J. E.; Kasemchainan, J.; Hartley, G. O.; Adamson, P.; Armstrong, D. E. J.; Marrow, J.; Bruce, P. G. Sodium/Na β″ Alumina Interface: Effect

of Pressure on Voids. *ACS Appl. Mater. Interfaces* **2020**, *12* (1), 678–685. https://doi.org/10.1021/acsami.9b17786.

(26) Dixit, M. B.; Verma, A.; Zaman, W.; Zhong, X.; Kenesei, P.; Park, J. S.; Almer, J.; Mukherjee, P. P.; Hatzell, K. B. Synchrotron Imaging of Pore Formation in Li Metal Solid-State Batteries Aided by Machine Learning. *ACS Appl. Energy Mater.* **2020**, *3* (10), 9534–9542. https://doi.org/10.1021/acsaem.0c02053.

(27) Krauskopf, T.; Mogwitz, B.; Rosenbach, C.; Zeier, W. G.; Janek, J. Diffusion Limitation of Lithium Metal and Li–Mg Alloy Anodes on LLZO Type Solid Electrolytes as a Function of Temperature and Pressure. *Adv. Energy Mater.* **2019**, *9* (44). https://doi.org/10.1002/aenm.201902568.

(28) Sudworth, J. L.; Tilley, A. R. *The Sodium Sulfur Battery*; Chapman & Hall, London, 1985.

(29) Zhang, X.; Wang, Q. J.; Harrison, K. L.; Roberts, S. A.; Harris, S. J. Pressure-Driven Interface Evolution in Solid-State Lithium Metal Batteries. *Cell Reports Phys. Sci.* **2020**, *1* (2), 100012. https://doi.org/10.1016/j.xcrp.2019.100012.

(30) Doux, J. M.; Nguyen, H.; Tan, D. H. S.; Banerjee, A.; Wang, X.; Wu, E. A.; Jo, C.; Yang, H.; Meng, Y. S. Stack Pressure Considerations for Room-Temperature All-Solid-State Lithium Metal Batteries. *Adv. Energy Mater.* **2020**, *10* (1), 1–6. https://doi.org/10.1002/aenm.201903253.

(31) Doux, J. M.; Yang, Y.; Tan, D. H. S.; Nguyen, H.; Wu, E. A.; Wang, X.; Banerjee, A.; Meng, Y. S. Pressure Effects on Sulfide Electrolytes for All Solid-State Batteries. *J. Mater. Chem. A* **2020**, *8* (10), 5049–5055. https://doi.org/10.1039/c9ta12889a.

(32) LePage, W. S.; Chen, Y.; Kazyak, E.; Chen, K.-H.; Sanchez, A. J.; Poli, A.; Arruda, E. M.; Thouless, M. D.; Dasgupta, N. P. Lithium Mechanics: Roles of Strain Rate and Temperature and Implications for Lithium Metal Batteries. *J. Electrochem. Soc.* **2019**, *166* (2), A89–A97. https://doi.org/10.1149/2.0221902jes.

(33) Zhou, Y.; Doerrer, C.; Kasemchainan, J.; Bruce, P. G.; Pasta, M.; Hardwick, L. Observation of Interfacial Degradation of Li_6PS_5Cl against Lithium Metal and $LiCoO_2$ via In Situ Electrochemical Raman Microscopy. *Batter. Supercaps* **2020**, 1–7. https://doi.org/10.1002/batt.201900218.

(34) Wenzel, S.; Sedlmaier, S. J.; Dietrich, C.; Zeier, W. G.; Janek, J. Interfacial Reactivity and Interphase Growth of Argyrodite Solid Electrolytes at Lithium Metal Electrodes. *Solid State Ionics* **2018**, *318* (July 2017), 102–112. https://doi.org/10.1016/j.ssi.2017.07.005.

(35) Lee, Y. G.; Fujiki, S.; Jung, C.; Suzuki, N.; Yashiro, N.; Omoda, R.; Ko, D. S.; Shiratsuchi, T.; Sugimoto, T.; Ryu, S.; Ku, J. H.; Watanabe, T.; Park, Y.; Aihara, Y.; Im, D.; Han I. T. High-Energy Long-Cycling All-Solid-State Lithium Metal Batteries Enabled by Silver–Carbon Composite Anodes. *Nat. Energy* **2020**, *5* (APril), 299–308. https://doi.org/10.1038/s41560-020-0575-z.

(36) Wang, M. J.; Carmona, E.; Gupta, A.; Albertus, P.; Sakamoto, J. Enabling "Lithium-Free" Manufacturing of Pure Lithium Metal Solid-State Batteries through in Situ Plating. *Nat. Commun.* **2020**, *11* (1), 1–9. https://doi.org/10.1038/s41467-020-19004-4.

(37) Koshikawa, H.; Matsuda, S.; Kamiya, K.; Miyayama, M.; Kubo, Y.; Uosaki, K.; Hashimoto, K.; Nakanishi, S. Dynamic Changes in Charge-Transfer Resistance at Li Metal/$Li_7La_3Zr_2O_{12}$ interfaces during Electrochemical Li Dissolution/Deposition Cycles. *J.*

Power Sources **2018**, *376*, 147–151. https://doi.org/10.1016/j.jpowsour.2017.11.082.

(38) Wu, B.; Wang, S.; Lochala, J.; Desrochers, D.; Liu, B.; Zhang, W.; Yang, J.; Xiao, J. The Role of the Solid Electrolyte Interphase Layer in Preventing Li Dendrite Growth in Solid-State Batteries. *Energy Environ. Sci.* **2018**, *11* (7), 1803–1810. https://doi.org/10.1039/c8ee00540k.

(39) Krauskopf, T.; Dippel, R.; Hartmann, H.; Peppler, K.; Mogwitz, B.; Richter, F. H.; Zeier, W. G.; Janek, J. Lithium-Metal Growth Kinetics on LLZO Garnet-Type Solid Electrolytes. *Joule* **2019**, *3* (8), 2030–2049.

(40) Albertus, P.; Babinec, S.; Litzelman, S.; Newman, A. Status and Challenges in Enabling the Lithium Metal Electrode for High-Energy and Low-Cost Rechargeable Batteries. *Nat. Energy* **2018**, *3* (1), 16–21. https://doi.org/10.1038/s41560-017-0047-2.

(41) Irvine, J. T. S. Electroceramics Characterized by Impedance Spectroscopy. *Adv. Mater.* **1990**, *2* (3), 132–138. https://doi.org/10.1002/adma.19900020304.

(42) Kraft, M. A.; Culver, S. P.; Calderon, M.; Böcher, F.; Krauskopf, T.; Senyshyn, A.; Dietrich, C.; Zevalkink, A.; Janek, J.; Zeier, W. G. Influence of Lattice Polarizability on the Ionic Conductivity in the Lithium Superionic Argyrodites Li_6PS_5X (X = Cl, Br, I). *J. Am. Chem. Soc.* **2017**, *139* (31), 10909–10918. https://doi.org/10.1021/jacs.7b06327.

(43) Adeli, P.; Bazak, J. D.; Park, K. H.; Kochetkov, I.; Huq, A.; Goward, G. R.; Nazar, L. F. Boosting Solid-State Diffusivity and Conductivity in Lithium Superionic Argyrodites by Halide Substitution. *Angew. Chemie - Int. Ed.* **2019**, *58* (26), 8681–8686. https://doi.org/10.1002/anie.201814222.

(44) Yu, C.; Ganapathy, S.; De Klerk, N. J. J.; Roslon, I.; Van Eck, E. R. H.; Kentgens, A. P. M.; Wagemaker, M. Unravelling Li-Ion Transport from Picoseconds to Seconds: Bulk versus Interfaces in an Argyrodite Li_6PS_5Cl-Li_2S All-Solid-State Li-Ion Battery. *J. Am. Chem. Soc.* **2016**, *138* (35), 11192–11201. https://doi.org/10.1021/jacs.6b05066.

(45) Boulineau, S.; Courty, M.; Tarascon, J. M.; Viallet, V. Mechanochemical Synthesis of Li-Argyrodite Li_6PS_5X (X = Cl, Br, I) as Sulfur-Based Solid Electrolytes for All Solid State Batteries Application. *Solid State Ionics* **2012**, *221*, 1–5. https://doi.org/10.1016/j.ssi.2012.06.008.

(46) Rao, R. P.; Adams, S. Studies of Lithium Argyrodite Solid Electrolytes for All-Solid-State Batteries. *Phys. Status Solidi Appl. Mater. Sci.* **2011**, *208* (8), 1804–1807. https://doi.org/10.1002/pssa.201001117.

(47) Deiseroth, H. J.; Maier, J.; Weichert, K.; Nickel, V.; Kong, S. T.; Reiner, C. Li_7PS_6 and Li_6PS_5X (X: Cl, Br, I): Possible Three-Dimensional Diffusion Pathways for Lithium Ions and Temperature Dependence of the Ionic Conductivity by Impedance Measurements. *Zeitschrift fur Anorg. und Allg. Chemie* **2011**, *637* (10), 1287–1294. https://doi.org/10.1002/zaac.201100158.

(48) Masias, A.; Felten, N.; Garcia-mendez, R.; Wolfenstine, J.; Sakamoto, J. Elastic, Plastic, and Creep Mechanical Properties of Lithium Metal. *J. Mater. Sci.* **2019**, *54* (3), 2585–2600. https://doi.org/10.1007/s10853-018-2971-3.

(49) Jow, T. R.; Liang, C. C. Interface between Solid Anode and Solid Electrolyte - Effect of Pressure on Li/LiI(Al_2O_3) Interface. *Solid State Ionics* **1983**, No. 9 & 10, 695–698.

(50) Yu, C.; van Eijck, L.; Ganapathy, S.; Wagemaker, M. Synthesis, Structure and Electrochemical Performance of the Argyrodite Li_6PS_5Cl Solid Electrolyte for Li-Ion Solid State Batteries. *Electrochim. Acta* **2016**, *215*, 93–99. https://doi.org/10.1016/j.electacta.2016.08.081.